doi:10.20944/preprints202210.0479.v1

Article

Surface versus Bulk State Transitions in Inkjet-Printed All-Inorganic Perovskite Quantum Dot Films

Thilini K. Ekanayaka,[1] Dylan Richmond,[2] Mason McCormick,[3] Shashank R. Nandyala,[4] Halle C. Helfrich,[5,6] Alexander Sinitskii,[3] Jon M. Pikal,[4] Carolina C. Ilie,[2] Peter A. Dowben [1] and Andrew J. Yost [5,7,*]

[1] Department of Physics and Astronomy, University of Nebraska-Lincoln, Lincoln, Nebraska 68588-0299, U.S.A.
[2] Department of Physics, State University of New York-Oswego, Oswego, New York 13126-3599, U.S.A.
[3] Department of Chemistry, University of Nebraska-Lincoln, Lincoln, Nebraska 68588-0304, U.S.A.
[4] Department of Electrical and Computer Engineering, University of Wyoming, Laramie, Wyoming 82071, U.S.A.
[5] Department of Physics, Oklahoma State University, Stillwater, Oklahoma, 74078, U.S.A.
[6] Department of Physics, Pittsburg State University, Pittsburg, Kansas 66762, U.S.A.
[7] Oklahoma Photovoltaic Research Institute, Oklahoma State University, Stillwater, Oklahoma, 74078, U.S.A.

* Correspondence: andrew.yost@okstate.edu

Abstract: Anion exchange of the halides, Br and I, is demonstrated through the direct mixing of two pure perovskite quantum dot solutions, $CsPbBr_3$ and $CsPbI_3$, and is shown to be both facile and result in a completely alloyed single phase mixed halide perovskite. Anion exchange is also observed in an interlayer printing method utilizing the pure, unalloyed perovskite solutions and a commercial inkjet printer. The halide exchange was confirmed by optical absorption spectroscopy, photoluminescent spectroscopy, X-ray diffraction, and X-ray photoemission spectroscopy characterization, and indicates that alloying is thermodynamically favorable, while the formation of a clustered alloy is not favored. Additionally, a surface-to-bulk photoemission core level transition is observed for the Cs 4d photoemission feature which indicates the electronic structure of the surface is different from the bulk. Time resolved photoluminescence spectroscopy indicates the presence of multiple excitonic decay features which is argued to originate from states residing at surface and bulk environments.

Keywords: Inkjet-printed perovskites, surface termination, $CsPbBr_3$, surface states, bulk states, trap states

1. Introduction

Hybrid halide and all-inorganic halide perovskite materials have attracted significant attention in the research community over the past decade [1–7]. The increased attention is due to their attractive material properties such as long carrier lifetimes [8,9], long diffusion lengths, [8,10] excellent device power conversion efficiency [11–13], and band gap tunability [14–17]. Both the hybrid and inorganic perovskites have shown some promise towards a number of potential applications such as lasers [18–22], photodetectors [23–25], high energy radiation detection [26,27], and of course in photovoltaics [6,28,29]. Although the hybrid halide perovskites show overall higher device power conversion efficiency, > 22% [30], when compared to the all-inorganic halide perovskites, > 13% [12], the hybrid halides suffer from light sensitivity/degradation and material instability due to environmental conditions [31]. The Pb based inorganic halide perovskites have an advantage over the hybrid halide perovskites because they show enhanced chemical stability and are overall more robust to environmental conditions [6,32–34]. When compared to traditional silicon based photovoltaic technology, the hybrid and all-inorganic perovskites have an advantage as they can be synthesized as high quality inks for low cost inkjet printing and the printed films retain the attractive performance features of the inks after printing [9,35–38].

In solar cell technology it is important to have high device performance with low fabrication costs. The use of photovoltaic inks in inkjet printing provides a low cost fabrication method with the ability to print high quality thin films in atmospheric conditions [38–40]. Additionally, inkjet printing can be used to rapidly prototype or combinatorically determine optimal materials combinations, and simultaneously act as a stepping stone to other large scale printing techniques, such as screen printing.

An attractive characteristic of these perovskites is the ease of which the bandgap can be tuned via small changes in the precursor stoichiometric ratios, also it can be tuned through halide exchange, making it an archetypal material for inkjet printing. As such, it is reasonable to assume two different single halide-based inks can be combined, both pre- and post- printing, in order to print custom mixed stoichiometric halide perovskite films, if alloy formation represents a thermodynamic sink that is sufficiently favorable to overcome barriers to interdiffusion.

Here we report the interlayer anion exchange in layer-by-layer inkjet printing of pure perovskite solutions and the presence of surface and bulk electron states in the printed films.

2. Materials and Methods

For a detailed procedure on the quantum dot ink synthesis the reader should refer to earlier works [9,37]. After synthesizing the quantum dot powders they were converted to inks for printing by dissolving, separately, 280 mg of $CsPbBr_3$ and $CsPbI_3$ powders in 25 mL of cyclohexane. The $CsPbBr_{3-x}I_x$ ink solution was prepared by combining a 1:1 mass ratio of $CsPbBr_3$ and $CsPbI_3$ ink solutions, known as direct mixing. Mixed inks ($CsPbBr_{3-x}I_x$) and pure inks ($CsPbBr_3$ and $CsPbI_3$) were printed on indium tin oxide (ITO) coated polyethylene terephthalate (PET) flexible substrates or amorphous glass substrates.

X-ray diffraction (XRD) was employed to investigate the crystal structure for all printed films using a Rigaku Smartlab diffractometer equipped with a Cu-Kα X-ray source with a wavelength of 1.54 Å. XRD is complemented by X-ray photoemission spectroscopy (XPS) to further establish composition of the photovoltaic printed films. XPS was performed with a SPECS Phoibos 150 hemispherical analyzer using non- monochromatized Al-Kα X-ray radiation and a pass energy of 15 eV. All XPS was performed at room temperature in an ultra-high vacuum chamber with a chamber pressure better than 5.0×10^{-10} mbar.

The optical absorption and photoluminescent properties of the quantum dot inks, single layer, and inter-layer printed films were measured using an Ocean Optics HR4000CG-UV-NIR high resolution spectrometer combined with an Ocean Optics DH-2000-BAL Deuterium-Halogen light source. Time resolved photoluminescence (TRPL) measurements were carried out at room temperature, on increasing thicknesses of CsPbBr3 single-layer printed films, using an ultrafast laser equipped with a Ti:Sa amplifier system that generates 4 mJ pulses at 800 nm with 100 fs pulse width and a repetition rate of 1 kHz. A portion of the 800 nm pulse is sent to an optical parametric amplifier to generate a 310 nm, 100 fs laser pulse. The sample PL was collected in a backscattering orientation with a high numerical aperture 90° off-axis parabolic mirror. The PL spectra were measured with an Avantes CCD spectrometer using a 325 nm long-pass filter to block the pump signal from entering the spectrometer. The measured PL spectra were corrected using a tungsten halogen lamp as a calibration source.

3. Results and Discussion

3.1. Structural and Optical Properties of Inks and Printed Films

In this experiment, three different printed layers are investigated as shown in Figure 1 (a)-(c): (1) printing single layer films of pure ($CsPbBr_3$ or $CsPbI_3$) and/or mixed perovskite $CsPbBr_3$-xIx inks, where the mixed perovskites have directly alloyed in solution from different anion nanoparticles, (single-layer printing), (2) printing successive layers of unalloyed $CsPbBr_3$ and $CsPbI_3$, one on top of the other (inter-layer printing), and (3) printing a thick layer (several layers) of $CsPbI_3$ onto a substrate followed by printing a thick layer of $CsPbBr_3$ on top of the $CsPbI_3$ layer (bi-layer printing).

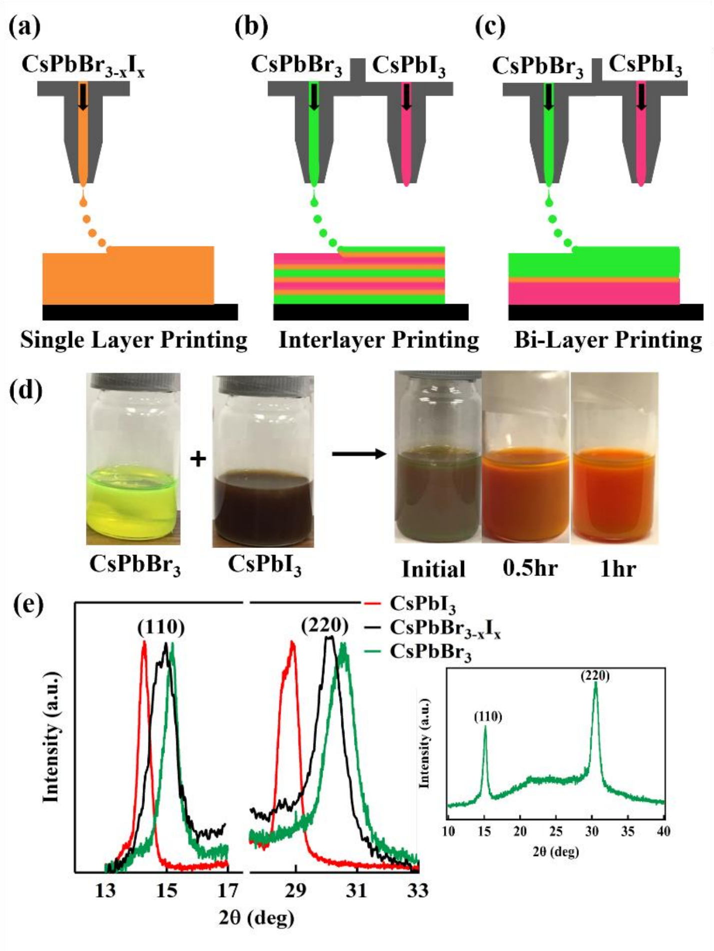

Figure 1: schematic of the printing methods employed where (a) is the single-layer method, (b) is the Inter-layer method, (c) is the bi-layer method, (d) (left) the image of pure $CsPbBr_3$ (yellow) and $CsPbI_3$(brown) inks. These inks are directly alloyed in solution from different anion (Br and I) nanoparticles, (right) accompanied by a color change over the course of one hour after mixing, (e) the XRD spectra for $CsPbI_3$ (red), $CsPbBr_{3-x}I_x$ (black), and $CsPbBr_3$ (green) single-layer printed films (after alloying of the nanoparticle in solution) indicating a lattice constant shift indicative of anion halide exchange, inset shows the typical orthorhombic crystal structure, characteristic of the printed perovskite nanoparticle films, with texturing along the (110) direction for all inks.

The direct mixed perovskite ($CsPbBr_3$-xIx) inks obtained from mixing the two pure $CsPbBr_3$ and $CsPbI_3$ quantum dot solutions is shown in Figure 1 (d). This alloying of the perovskite nanoparticles occurred in solution at room temperature without any temperature treatment or other further efforts to aid the process (like stirring). Figure 1(d) shows how the color of the quantum dot ink mixture changes from brown to orange with time, a signature of the material resolving into an alloy of intermediate band gap. The color change is believed to be due to an anion exchange whereby the Br and I ions migrate within the pure perovskite solutions to form a new mixed perovskite [41]. The alloying process takes approximately 30 minutes to 1 hour, however for larger nanoparticles the alloying process may be on a different time scale and requires further consideration.

$CsPbX_3$ quantum dots have been shown to be more ionic in nature and in their interactions with ligands which suggests an ionic migration mechanism [42]. Indeed, it has been shown that inorganic halide perovskites have high ionic conductivities due to anion migration and exchange/replacement of the halide ions in these perovskites is facile [41,43,44]. Thus, when mixing two pure, unalloyed perovskite quantum dot solutions, the nanoparticle alloy formation is likely facilitated by anionic migration and to some extent by the free ligands present in the solution [41,42]. The ease and rapidity of the halide exchange/alloying indicates this is thermodynamically favorable.

The structure changes, accompanying the nanoparticle mixed anion alloy formation, as characterized by X-ray diffraction (XRD) are consistent with a single phase material. The XRD patterns for the single-layer printed films of pure $CsPbX_3$ quantum dots and the direct mixed $CsPbBr_3$-xIx quantum dots are shown in Figure 1(e) indicating a crystal structure in the orthorhombic phase at room temperature in agreement with literature [45–47]. The (110) and (220) peaks of the mixed perovskite show a peak shift compared to the peaks of the pure perovskites which indicates a lattice constant change. The lattice constants for $CsPbBr_3$ are a=8.207 Å, b=8.355 Å and c=11.759 Å, and for $CsPbI_3$ they are a= 8.8561 Å, b= 8.6361 Å and c= 12.4722 Å. For the $CsPbBr_3$-xIx the lattice constants are a= 8.5316Å, b= 8.2158 Å and c= 12.1156 Å. Thus, by mixing two pure perovskites inks we can obtain a completely alloyed solution with a lattice constant which falls between the pure (unalloyed) perovskites. The absence of peaks representative of $CsPbBr_3$ and $CsPbI_3$ in the XRD data of $CsPbBr_3$-xIx also suggests the absence of $CsPbBr_3$ and $CsPbI_3$ clusters within the mixed perovskite. The quantum dot sizes for the pure and mixed perovskites were calculated using the Scherrer equation [48] and a standard Lorentzian distribution fitting function of the (220) Bragg peak. The quantum dot sizes (diameters) for all CsPbX3 were determined to be roughly 6 - 7 nm. As a comparison, CsPbBr3 nanoparticles were determined to be around 7.3 ± 1.0 nm using TEM, see supporting information, in good agreement with the XRD calculations. This indicates the halide exchange in direct mixing of pure perovskite solutions does not affect the quantum dot particle size significantly. This surprising retention of nanoparticle size agrees with a study performed by Akkerman et al [41]. Interestingly, the XRD peaks, of the directly mixed perovskite, from a mixed nanoparticle solution, appear closer to the $CsPbBr_3$ diffraction peak placement than $CsPbI_3$. This indicates that the direct mixed perovskite is heavily weighted towards a large Br anion concentration.

The structural changes of the mixed anion alloy nanoparticle is consistent with the changes in the optical properties. The $CsPbBr_3$-xIx inks and the printed films are highly luminescent, displaying vivid colors, as shown in Figure 2 (a), suggesting the optical properties have been tuned to span a broad color spectrum. The optical absorption and background subtracted photoluminescence spectra of the pure CsPbBr3 and CsPbI3 and the direct mixed $CsPbBr_3$-xIx quantum dot single-layer printed films are shown in Figure 2 (b) and (c), respectively. The absorption spectra, Figure 2 (b), for the pure $CsPbBr_3$ film indicates absorption onsets around 499 ± 2 nm and $CsPbI_3$ quantum dot printed film indicates strong absorption all over the visible region in agreement with literature [16,41]. The optical absorption onset, which appears around 542 ± 3 nm for the printed films from alloy $CsPbBr_3$-xIx quantum dots (directly alloyed in solution from different anion (Br and I) nanoparticles). This optical absorption for the printed films, from alloy $CsPbBr_3$-xIx quantum dots, is located between the absorption onsets of the pure (unalloyed) $CsPbBr_3$ and $CsPbI_3$ quantum dot films. The photoluminescent spectra, Figure 2 (c), of pure $CsPbBr_3$ and $CsPbI_3$ quantum dot printed films shows peaks around 504 ± 1 nm and 691 ± 2 nm, respectively, in agreement with the literature [41]. The photoluminescent peak for the alloyed $CsPbBr_{3-x}I_x$ quantum dot printed films, following formation from the mixed nanoparticle solutions, appears at 546 ± 4 nm, which again falls between the pure (unalloyed) quantum dot printed films. The absorption and photoluminescent data provide no indication of clustering of either $CsPbBr_3$ or $CsPbI_3$ in the direct mixed $CsPbBr_{3-x}I_x$ single-layer printed films. As the direct mixed $CsPbBr_{3-x}I_x$ quantum dot printed films exhibit absorption onsets and photoluminescent peaks falling between those of the pure perovskite films and somewhat closer to the $CsPbBr_3$ films, in agreement with XRD, these data suggest that anion exchange produces an alloyed single phase perovskite while again supporting the idea that the direct mixed perovskite is heavily weighted towards a higher Br anion concentration.

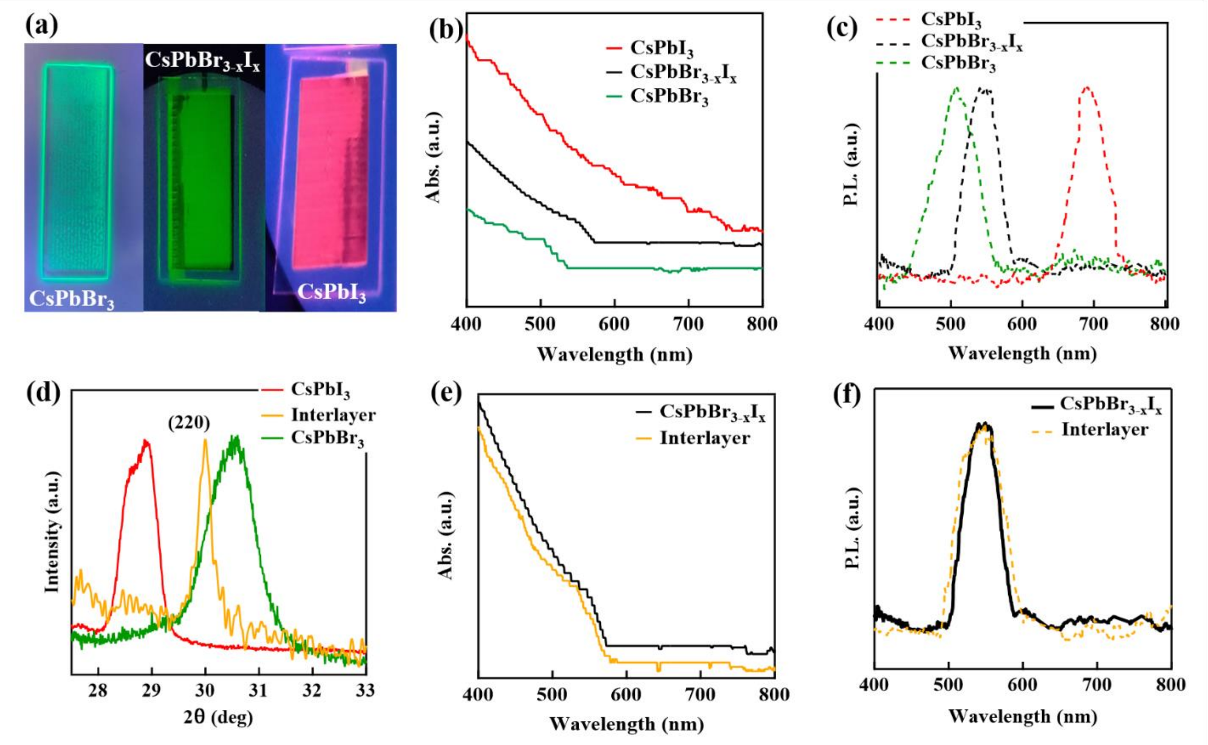

Figure 2: (a) image of printed films of pure nanoparticle solutions and alloyed nanoparticle perovskite solution under UV light, (b) optical absorption spectra obtained for printed films of $CsPbBr_3$, $CsPbI_3$ and $CsPbBr_{3-x}I_x$.,(c) background subtracted photoluminescence spectra obtained for printed films of $CsPbBr_3$, $CsPbI_3$ and $CsPbBr_3$, (d) the XRD spectra of printed films, from the pure $CsPbBr_3$ and $CsPbI_3$ single-layer printed films , compared to the inter-layer printed film (denoted interlayer), indicating a lattice constant shift due alloying mediated by halide exchange, (e) the optical absorption spectra and (f) the photoluminescence spectra of alloyed $CsPbBr_{3-x}I_x$ perovskite single-layer printed film, compared to the inter-layer printed film (denoted interlayer).

3.2. Nanoparticle Alloying by Anion Exchange across an Inter-layer Printed Film Interface

In the interest of ascertaining and confirming that alloying is favored across the interface between different anions in the printed films, an inter-layer printing technique was employed by printing alternating layers of pure $CsPbBr_3$ and $CsPbI_3$, beginning with a layer of $CsPbI_3$, see Figure 1. Figure 2 (d) shows a comparison of the XRD data for printed films of the $CsPbBr_3$, $CsPbI_3$, and an inter-layer printed film prepared by the sequential printing of layers from the pure $CsPbBr_3$ and $CsPbI_3$ nanoparticle inks. There is a clear indication of alloying across the interlayer. This inter-layer printing method results in interdiffusion across the interface of the $CsPbBr_3$ and $CsPbI_3$ heterolayers. Interestingly, the (220) and (110) Bragg peaks of the interlayer printed film, as with the direct mixed $CsPbBr_{3-x}I_x$ single-layer printed films, again fall between the (220) and (110) peaks of the pure (unalloyed) $CsPbBr_3$ and $CsPbI_3$ films indicating that there is a lattice constant shift due to anion exchange between the interdiffused layers of $CsPbBr_3$ and $CsPbI_3$. The optical absorption and photoluminescent spectra of the inter-layer printed films (denoted inter-layer, in Figure 2 (e) and (f)) are compared to those of the direct mixed $CsPbBr_{3-x}I_x$ single-layer printed quantum dot film, indicating close agreement.

There exists the possibility of limitations to alloying of the heterolayer Br and I anion nanoparticle perovskite inter-layer printed films which could be consistent with either a higher barrier to interdiffusion or limits to diffusion lengths and rates once printed. These limitations to alloying once the perovskite films are printed were tested using the bi-layer printing method where a thick layer of $CsPbBr_3$ is printed and then a thick layer of $CsPbI_3$ is printed on top of the $CsPbBr_3$ films. The photoluminescent spectrum, see supplementary Figure S1, suggests the thicker bi-layer printing method results in unmixed, phase separated, components rather than a uniform alloyed mixed $CsPbBr_{3-x}I_x$ perovskite film as seen in the thinner inter-layer printed films, where inter-layer mixing is more uniform (Figure 2(d)-(f)), and single-layer printed films made from mixing pure nanoparticle solutions (Figure 2(a)-(c)).

In both the single-layer printed alloyed quantum dots film, from mixing pure nanoparticle solutions, and the inter-layer printed film, with mixing occurring at the interfaces, the end result was a material where a final mixed halide state is seen to be strongly preferred. In other words, when mixed together, either in solution or as a heterolayer system, the $CsPbBr_{3-x}I_x$ perovskites prefer to exist as a single phase mixed alloy rather than remain phase separated, i.e. strongly clustering. The data from single-layer printed film, from mixing pure nanoparticle solutions prior to printing, and the inter-layer printed films, with mixing occurring at the interfaces, suggest that the mixed state acts as a thermodynamic sink and provides a minimum in the energy landscape during the reaction phase of the halide exchange. The thicker bi-layer system is an exception, as seen in supporting information, as this retains some separation of the stacked $CsPbBr_3$ and $CsPbI_3$ films, which could be due to the increased layer thickness and/or rapid solvent evaporation acting as limiting factors in the halide exchange reaction and hetero-layer interdiffusion process.

3.3. Surface-to-Bulk Core Level Shift

One can imagine, upon completion of anion (halide) exchange to form a new alloy ($CsPbBr_{3-x}I_x$), the possibility of electronic surface state and bulk states which are very different from those in non-alloyed ($CsPbBr_3$ or $CsPbI_3$) materials is likely. Additionally, the surface could exhibit an electronic structure different from the bulk which may be observable in angular dependent photoemission spectroscopy.

Interestingly, a surface-to-bulk core level shift [49–51] was observed for the Cs 4d core level XPS feature, for both the CsPbBr3 and the alloy $CsPbBr_{3-x}I_x$ single-layer printed films, the latter of which forms from the direct mixing of the different anion nanoparticles in solution prior to printing, as shown in Figure 3 (a) and (b), respectively. In order to increase the surface sensitivity of XPS, the photoemitted electron take-off angle was varied from 0° to 40°. By increasing the take-off angle of the emitted electrons from 0° to 40°, the intensity of a surface contribution will appear to increase in intensity relative to the bulk contribution [49,50]. In Figure 3 (a) and (b), curve A (red dots) corresponds to a photoemitted electron takeoff angle of 40° and curve B (black triangles) corresponds to a takeoff angle of 0°, with respect to the surface normal. Beneath each curve the surface (dashed lines) and bulk (solid lines) contribution fittings are displayed. The intensity difference, curve C, between curve A and curve B is plotted as a solid green line.

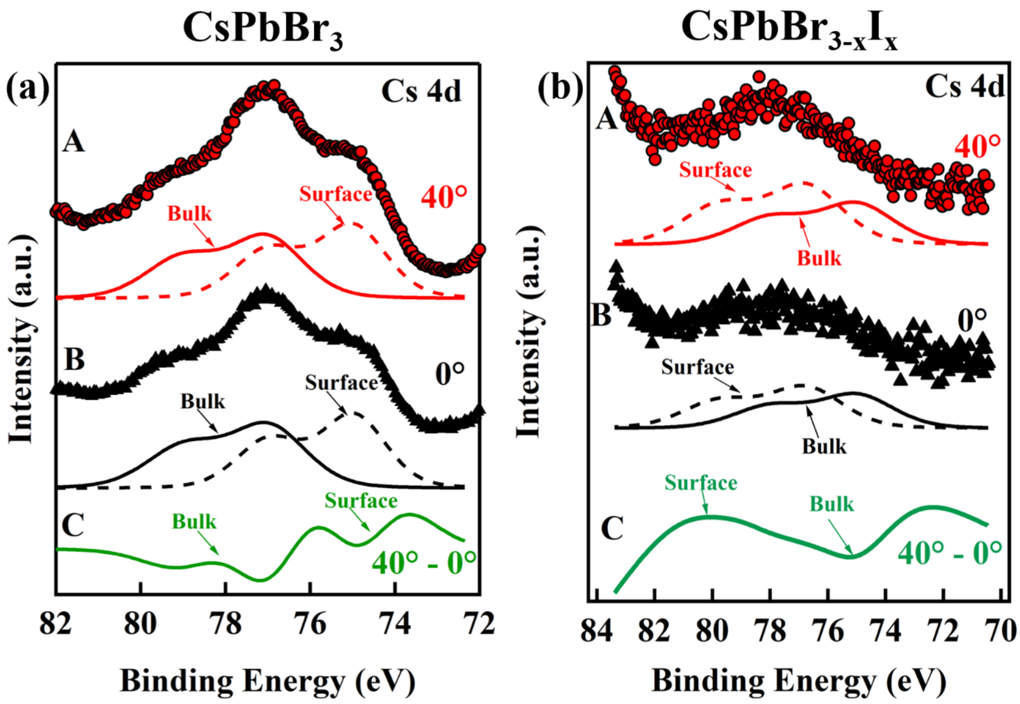

Figure 3 The Cs 4d core level X-ray photoelectron spectroscopy features of the single layer printed (a) $CsPbBr_3$ and (b) $CsPbBr_{3-x}I_x$. Notice: curve A is spectrum taken at emission takeoff angle of 40°,with respect to the surface normal, the surface and bulk fitted curves of curve A are beneath; curve B is spectrum taken at emission takeoff angle of 0°, i.e. along the surface normal, with the surface and bulk fitted curves of curve B are beneath; curve C is the intensity difference between A and B indicating the surface contribution and the bulk contribution of the surface-to-bulk core level shift

As shown in Figure 3, both films ($CsPbBr_3$ and $CsPbBr_3$-xIx) exhibit increases in their respective photoemission intensity i.e. surface states which emerge with increasing take-off angle. If one considers the intensity difference curve, curve C (solid green line), then for $CsPbBr_3$ curve C indicates the surface contribution is a broad peak at lower binding energy and the bulk contribution is a dip at higher binding energy. In comparison, curve C for $CsPbBr_3$-xIx films, indicates the surface contribution is a broad peak at higher binding energy than the bulk contribution (dip) at lower binding energy. The appearance of a surface state at low binding energy in $CsPbBr_3$ and at high binding energy in $CsPbBr_3$-xI_3 suggests that the surface terminations are different for the quantum dot films.

The X-ray photoemission (XPS), shown in supplementary Figure S2, was utilized in order to investigate the composition of the $CsPbBr_3$-xIx quantum dot printed films, formed after mixing the different anion nanoparticle solutions. The Cs $3d_{5/2}$ and $3d_{3/2}$ core level photoemission peaks are located at 723.8 ± 0.2 eV and 737.88 ± 0.2 eV, respectively. The Pb $4f_{7/2}$ and $4f_{3/2}$ core level peaks are located at 138.1 ± 0.1 eV and 142.9 ± 0.2 eV, respectively. While surface segregation of metallic Pb in lead halide perovskites is a well-established phenomenon [52–57], no evidence of Pb^0 clusters at the film surface was evident in core level photoemission spectra at the Pb core level photoemission features. The XPS spectra of Br shows up as a single broad photoemission peak centered around 68 eV, with an additional feature at higher binding energies, due to the Cs 4d core level feature. A modified Voigt function was used to fit the broad Br core level peak and peak positions for Br $3d_{5/2}$ and $3d_{3/2}$ were extracted and determined to be 68.1 ± 0.2 eV and 69.6 ± 0.2 eV, respectively. The core level photoemission features of I $3d_{5/2}$ and I $3d_{3/2}$ are located at 618.4 ± 0.2 eV and 629.9 ± 0.2 eV, respectively. All of the core level photoemission features for

Cs, Pb, I, and Br agree well with values reported in literature for $CsPbBr_3$, $CsPbI_3$ and mixed perovskites [34,47,58–60]. The photoemission intensities were used to calculate a Br:I atomic ratio of roughly 2.4:0.6, suggesting a Br weighted direct mixed perovskite, $CsPbBr_{2.4}I_{0.6}$, in agreement with the XRD, optical absorption spectroscopy, and photoluminescent spectroscopy data. The XPS of the Cs 4d and Pb $4f_{7/2}$ and $4f_{3/2}$ core level photoemission features provide further evidence that halide clustering, in the alloy, does not occur, as there are no satellite features which are common in Cs-halide clustered materials [61,62]. Cs-halide free clusters are also unlikely. The Cs lattice atom can exist in only one oxidation state, in a lattice with large electron affinity anions, suggesting that the surface-to-bulk core level shift is attributable to a large difference in the electronic structure of the surface versus the bulk of the thin films. Furthermore, there is a large separation in the binding energies of the surface versus bulk peaks confirming the idea that the surface electronic structure is vastly different from the bulk [51].

3.4. Transient Recombination Measurements

The presence of defects and trap states in these materials is well known and one could postulate, with confidence, with the presence of surface-to-bulk transitions that defects/trap states located near the surface may be different, with respect to the excitonic recombination time, than defect/trap states located within the bulk of the material/film. Indeed, in previous work on these materials the transport data and drift carrier lifetimes indicated regions of fast and slow recombination [9], which suggests the presence of at least two recombination pathways and possibly more. Multiple excitonic recombination pathways and energy loss mechanisms would cause the TRPL profile to broaden along the time axis especially if these states have a strong influence on the exciton recombination [63]. The origins of multiple recombination lifetimes regarding these materials is somewhat ambiguous, moreover there seems to be little consensus in the literature on established lifetime ranges.

A list of recent TRPL studies on $CsPbBr_3$ and $CsPbBr_{3-x}I_x$ along with the decay times and postulated origins for those lifetimes are contained in Table 1. Something to notice before discussing the postulated origins, not all of the studies have listed multiple decay event lifetimes, some have one lifetime and others only two or three. Limiting the fitting equations to one or two term exponential equations results in the data fits being too high in the data and/or too low in the data along the vertical axis. This poses a problem for the correct interpretation of the TRPL data and whether or not those fits (single and two term exponential equations) represent the system correctly. Looking carefully at Table 1 the reader can notice that the majority of the postulated origins of transient events can be broken down into the following types: surface states, bulk states, traps states, radiative recombination, and non-radiative recombination. Multiple origins for recombination events across similar systems leads credence to the idea that the fitting equations need to account for more than two events in any given system, especially if said system is capable of multiple energy transitions from the excited state as has been suggested for inorganic lead halides [64]. Another cause for concern is related to the time-ranges for the various postulated origins, which all seem to overlap at least for the cases presented in Table 1. It may be more instructive to focus on the surface and bulk state times associated only with $CsPbBr_3$. The time coonstant range for surface states is $\tau_{surface}$ = 1.22-23 ns and for bulk states the range is τ_{bulk} = 3.55-233 ns, clearly there is some overlap again. If one considers the average of the lifetimes, rather than the time-range, then recombination due to surface states is roughly 12 ns and bulk states is roughly 118 ns. We then can say with some

Material	τ_1	Origin for τ_1	τ_2	Origin for τ_2	τ_3	Origin for τ_3
CsPbBr$_3$(300K) QDs[71]	3.64 ns	free exciton	8.16 ns	localized exciton		
CsPbBr$_3$(300K) QDs[72]	6.44 ns	single exciton transition				
CsPbBr$_3$(4K) QDs[72]	355 ps	bright state emission	5.75 ns	lower lying dark state		
CsPbBr$_3$ Single Crystal[73]	23 ns	surface state	233 ns	bulk state		
CsPbBr$_3$[74]	7.6 ns	non-radiative recombination	55.9 ns	radiative recombination		
CsPbBr$_3$[75]	1.22 ns	surface state	3.55 ns	bulk state		
CsPbBr/I$_3$[75]	1.7 ns	surface state	11.78 ns	bulk state		
CsPbBr/I$_3$[75]	2.31 ns	surface state	50.39 ns	bulk state		
CsPbBr$_3$[76]	3.8 ns	excitonic recombination	17.6 ns	trap state		
CsPbBr$_3$ NCs(4.6nm size) [77]	0.19 ns	trap state	4.1 ns	radiative recombination of single exciton		
CsPbBr$_3$ NCs(9.4nm size) [77]	0.43 ns	trap state	6.0 ns	radiative recombination of single exciton		
CsPbBr$_3$ NCs(11.4nm size)[77]	11.4 ns	radiative recombination of single exciton				
CsPbBr$_3$ qds (220K)[78]	0.193 ns	excitonic recombination				
CsPbBr$_3$[79]	13 ns	x	69 ns	x		
CsPbBr$_3$ solution NCs[80]	0.87 ns	x	5.8 ns	x	50 ns	charge trapping
CsPbBr$_3$ film NCs[80]	0.93 ns	x	42 ns	charge trapping		
CsPbBr$_3$[81]	4.68 ns	x	22.93 ns	x	140.52 ns	x
CsPbBr/I$_3$[81]	17.09 ns	x	67.71 ns	x	251.63 ns	x
Al:CsPbBr$_3$[81]	5.11 ns	x	34.82 ns	x	139.7 ns	x
Al:CsPbBr/I$_3$[81]	10.52 ns	x	39.97 ns	x	226.2 ns	x
CsPbBr$_3$ QDs solution(hexane)[82]	12.3 ns	x	42.4 ns	x	189.0 ns	x
CsPbBr$_3$ QDs film(hexane)[82]	1.35 ns	x	5.11 ns	x	19.8 ns	x

Table 1: *List of some recent TRPL measurements for* $CsPbBr_3$ *and* $CsPbBr_{3-x}I_x$ *materials. Column 1, labeled 'Material', indicates the type of material investigated along with reference number. Columns 2, 4, and 6 , labeled '*τ_1*', '*τ_2*', '*τ_3*', respectively are the TRPL lifetimes measured in the associated studies. Columns 3, 5, and 7, labeled 'origin of* τ_1*', 'origin of* τ_2*', 'origin of* τ_3*', respectively, are the physical origin of the lifetimes in columns 2, 4, and 6, respectively, according to the associated reference.*

confidence that typically $\tau_{surface} < \tau_{bulk}$. As trap states can exist at the surface and in the bulk, it is proposed that there should be four possible decay events that would correspond to surface-trap, surface, bulk-trap, and bulk like states such that $\tau_{surface} < \tau_{surfacetrap} < \tau_{bulk} < \tau_{bulktrap}$. In this scenario, it is assumed that trap states (shallow) are long lived states that do not promote recombination, although it is acknowledged that deep trap states may exist and would promote fast recombination.

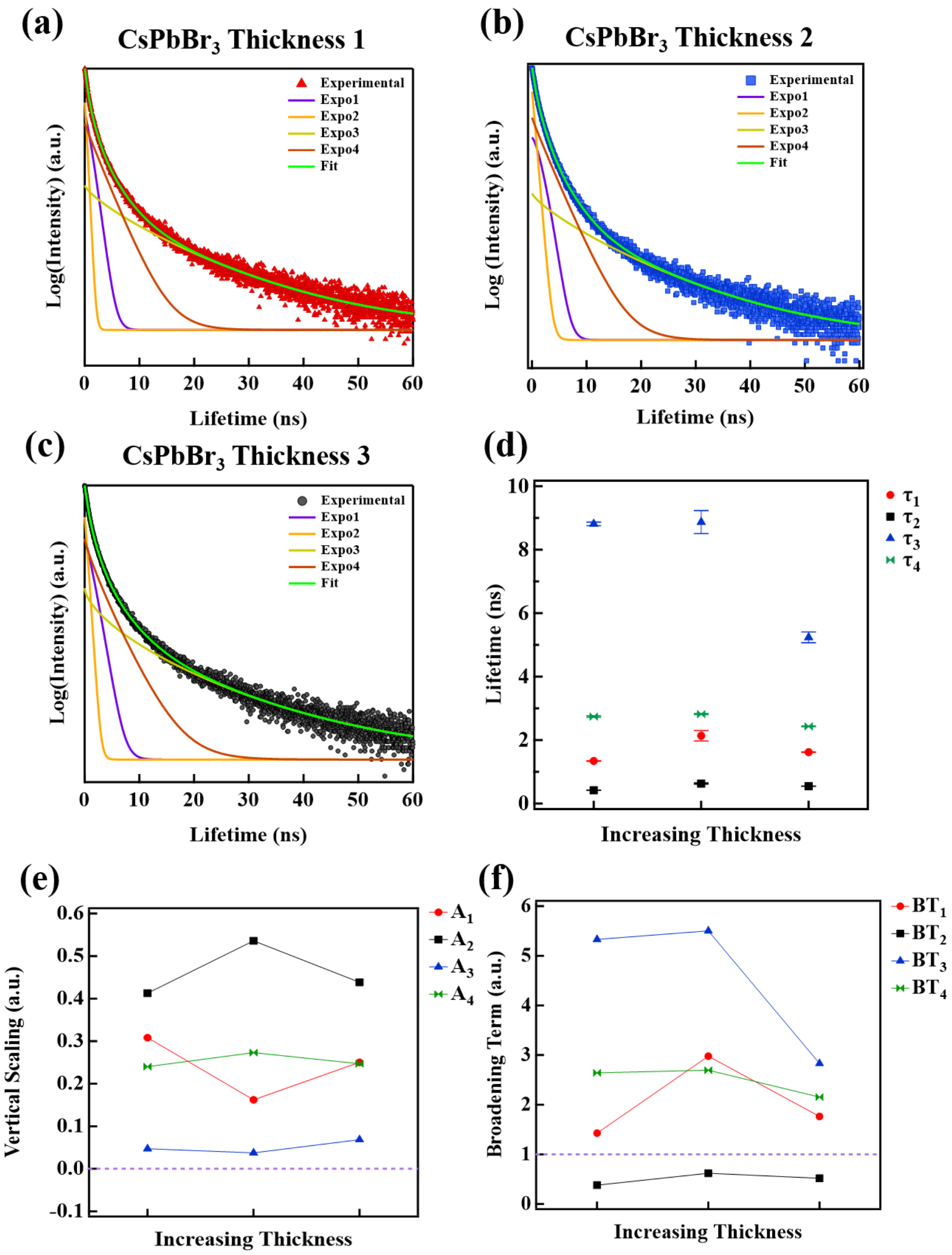

Figure 4: *(a) TRPL spectra for single-layer method of CsPbBr*$_3$ *films of thickness 1 (red triangles), (b) thickness 2 (blue squares), (c) thickness 3(black circles), such that thickness 1 < thickness 2 < thickness 3. Notice in each plot (a)-(c) the exponential subpeaks Expo1-4, are overplotted and equation (1) fitting equation is overplotted on the data (green curve)., (d) the extracted time constants vs layer thickness, life-times* τ_1*(red line-circle),* τ_2*(black line-square),* τ_3*(blue line-triangle),* τ_4*(green line-hourglass) are from fitting equation (1) in (a)-(c), (e) vertical scaling constants vs layer thickness, the scaling constants* A_1*(red line-circle),* A_2*(black line-square),* A_3*(blue line-triangle),* A_4*(green line-hourglass) are from fitting equation (1) in (a)-(c), (f) broadening term vs layer thickness, the broadening term as defined by equation (2) is extracted from the fitting equation (1) in (a)-(c) .*

TRPL measurements for CsPbBr$_3$ films of increasing thickness are shown in Figure 4 (a)-(c). The TRPL profiles exhibit a broad exponential decay profile which suggests that regular exponential decay functions may not describe the events properly. Indeed single, double and triple regular and stretched exponential functions cannot be used to confidently fit the data. A least squares fitting method was employed with the following quadruple stretched exponential equation:

Preprints (www.preprints.org) | NOT PEER-REVIEWED | Posted: 31 October 2022 doi:10.20944/preprints202210.0479.v1

$$f(t) = A_1 e^{-\left(\frac{t}{\tau_1}\right)^{\beta_1}} + A_2 e^{-\left(\frac{t}{\tau_2}\right)^{\beta_2}} + A_3 e^{-\left(\frac{t}{\tau_3}\right)^{\beta_3}} + A_4 e^{-\left(\frac{t}{\tau_4}\right)^{\beta_4}} + c \qquad (1)$$

where, A_1-A_4 are the weighted contribution terms which describe relative importance of the exponential terms and thus the prevalence of a recombination event. The lifetimes, τ_1-τ_4, correspond to the recombination lifetimes of the exciton recombination events. The power terms, β_1-β_4, influence the horizontal broadening of the exponential terms.c represents the vertical shift of equation 1, rather the noise floor of the TRPL signal.

The associated recombination lifetimes for the $CsPbBr_3$ films where the single-layer printing method is used, are extracted from the fittings using equation (1) and plotted versus increasing film thickness in Figure 4 (d). All lifetime curves are distinct, with respect to the error bars, for all sample thicknesses meaning none of the curves intersect or overlap.

Interestingly, the lifetime curves seem to group into two regions namely fast and slow recombination time regions where for fast recombination $\tau < 4.0$ ns (includes τ_1, τ_2, and τ_4) and for slow recombination $\tau > 4.0$ ns (includes τ_3). The lifetime curves in the fast recombination region (τ_1, τ_2, and τ_4) have a mostly constant slope, independent of layer thickness whereas the lifetime curve in the slow recombination region (τ_3) begins to reduce with increasing thickness. If one considers the average of the lifetimes for each τ_i curve such that $\tau_{avg1} = 1.70$ ns, $\tau_{avg2} = 0.53$ ns, $\tau_{avg3} = 7.64$ ns, $\tau_{avg4} = 2.66$ ns. In other words, the lifetimes indicate that $\tau_{avg2} < \tau_{avg1} < \tau_{avg4} < \tau_{avg3}$. Surface states are theorized to promote recombination due to the abrupt termination of the crystal lattice [65–67], as such the fastest lifetimes are likely associated with surface related recombination. By convention of the proposed model, where $\tau_{surface} < \tau_{surfacetrap} < \tau_{bulk} < \tau_{bulktrap}$, assignment of the average lifetimes would follow as $\tau_{surface} = \tau_{avg2}$; $\tau_{surfacetrap} = \tau_{avg1}$; $\tau_{bulk} = \tau_{avg4}$; $\tau_{bulktrap} = \tau_{avg3}$.

The weighted contributions to the TRPL spectra are described by the A_i terms in equation (1). The A_i for each exponential subpeak term versus film thickness are plotted in figure 4 (e). The Ai indicates, for each τi, the overall contribution to the fit function, contained within the decay profiles shown in figures 4(a)-(c). Furthermore, the A_i term mathematically indicates the extent of vertical stretching or vertical compressing along the intensity axis for each exponential subpeak of equation (1) such that if $A_i > 0.0$ a vertical stretching occurs and if $A_i < 0.0$ a vertical compression results. All weighting term curves in figure 4 (c) are greater than 0.0 for all thicknesses, meaning they all contribute to a vertical stretching of the fitting function, equation (1). For the most part, the weighting term curves do not vary appreciably with increasing film thickness. A_2 (black line-square) and A_3 (blue line-triangle) are well separated from A_1 (red line-circle) and A_4 (green line-hourglass). The weighted term averages are as follows: $A_{avg1} = 0.24$, $A_{avg2} = 0.46$, $A_{avg3} = 0.05$, and $A_{avg4} = 0.25$. This would make the average A_i weighting term inequality appear as $A_{avg3} < A_{avg1} < A_{avg4} < A_{avg2}$. Due to the dominate nature of the surfaces state contributions to the photoluminescence decay profiles [68–70], it is expected that surface related recombination events should have the largest A_i terms on average. Additionally, it is expected that trap related states will have less density compared to their counterpart states (surface and bulk) and should have smaller weighting term contributions accordingly. Applying these guidelines to the weighting terms leads to the following model-based inequality, $A_{bulktrap} <$, $A_{bulk} < A_{surfacetrap} < A_{surface}$, which is similar to the model-based lifetime inequality, $\tau_{surface} < \tau_{surfacetrap} < \tau_{bulk} < \tau_{bulktrap}$, except the subscripts are in reverse order. If we use the model-based weighting term inequality as a guide then assignments of the average weighting terms are as follows $A_{surface} = A_{avg2}$; $A_{surfacetrap} = A_{avg1}$; $A_{bulk} = A_{avg4}$; $A_{bulktrap} = A_{avg3}$.

The extended broadening along the time axis, as is apparent in the TRPL data of Figures 4 (a)-(c), is a major source of error in most TRPL fittings if left unaccounted for in the fitting function. It is also challenging to establish a single source or physical process responsible for the broadening due to the complexities inherent in the exciton formation and subsequent recombination process. Once an exciton is formed there exists radiative and non-radiative interactions and as such associated recombination and charge transfer rates [63]. Non-radiative interactions that may or may not induce recombination can delay or expedite the eventual recombination of the exciton. The temporal delay leads to a broadening or horizontal stretching along the time axis in TRPL spectra. The broadening terms for each exponential subpeak from equation (1) versus increasing film thickness are plotted in Figure 4 (f). In this study the broadening term is defined as follows:

$$BT_i = {\tau_i}^{\beta_i} \tag{2}$$

where τ_i is the lifetime term from the TRPL fitting equation, equation (1), see Figure 4 (d). β_i is the power of the exponential power in equation (1). If BT_i is > 1.0 then a horizontal stretching (broadening) occurs whereas if BT_i < 1.0 then horizontal compression ensues. For all film thicknesses, the BT_1, BT_3, and BT_4 terms are greater than 1.0 suggesting they add to the horizontal broadening. Whereas, the BT_2 is less than 1.0, for all thicknesses, which means this acts to compress the fitting curve, similar to a fast recombination process with negligible delay before recombination. If we assume that short delay or fast recombination processes contribute less broadening than the slow recombination processes, then a model-based broadening term inequality can be established such that $BT_{surface} < BT_{surfacetrap} < BT_{bulk} < BT_{bulktrap}$. This is similar to the model-based lifetime inequality, $\tau_{surface} < \tau_{surfacetrap} < \tau_{bulk} < \tau_{bulktrap}$. On average the broadening terms are $BT_{avg1} = 1.97$, $BT_{avg2} = 0.51$, $BT_{avg3} = 4.38$, $BT_{avg4} = 2.48$, such that $BT_{avg2} < BT_{avg1} < BT_{avg4} < BT_{avg3}$. If we use the model-based broadening term inequality as a guide then assignments of the average broadening terms are as follows $BT_{surface} = BT_{avg2}$; $BT_{surfacetrap} = BT_{avg1}$; $BT_{bulk} = BT_{avg4}$; $BT_{bulktrap} = BT_{avg3}$.

All of the fitting constants are consistent in their identification of the proposed process. These findings are extremely important in the context of the debate regarding the existence and role of surface and bulk states in the charge transport properties of $CsPbX_3$ photovoltaic cells. More measurements are necessary to explore the role of phonon coupling and the chemical nature of the trap states in these materials.

4. Conclusions

This study demonstrates anion exchange of $CsPbBr_3$ and $CsPbI_3$ solutions/films results in high quality alloyed $CsPbBr_{3-x}I_x$ nanoparticle textured thin films, through both direct mixing of nanoparticles in solution and heterolayer printed films, with mixing occurring at the interlayer. The halide exchange in both methods results in a single phase completely alloyed mixed perovskite as confirmed by XRD, optical absorption spectroscopy, photoluminescent spectroscopy, and X-ray photoemission spectroscopy. The mixed halide state acts as a thermodynamic sink providing a minimum in the energy landscape of the halide anion exchange reaction. Additionally, the electronic structure of the film surface is shown to be very different compared to the bulk through the observation of a surface-to-bulk core level shift. The efficacy of inkjet printing, as it applies to combinatoric studies and rapid prototyping has been realized.

Supplementary Materials: The following supporting information can be downloaded at: www.mdpi.com/xxx/s1, Figure S1:TEM image of the $CsPbBr_3$ quantum dots with average size of 7.3 nm.; Figure S2: Photoluminescence of the bi-layer $CsPbBr_3/CsPbI_3$ quantum dot printed thin film, the presence of two separate peaks located at roughly 490 nm and 650 nm suggests the presence of segregated $CsPbBr_3$ (green line) and $CsPbI_3$ (red line), thus confirming the bi-layer printing method results in unmixed layers of $CsPbBr_3/CsPbI_3$; Figure S3: X-ray photoelectron spectroscopy of (a) the Cs 3d core level peaks, (b) Pb 4f core level peaks, and (c) the Br 3d core level peaks and Cs 4d core level peaks and (d) the I 3d core level peaks for the direct mixed perovskite $CsPbBr_{2.4}I_{0.6}$ quantum dot printed thin films; Figure S4: Optical absorption and photoluminescence profiles for $CsPbBr_3$ films, printed with single-layer printing method, of (a) thickness 1, (b) thickness 2, and (c) thickness 3.

Author Contributions: Conceptualization, A.J.Y. and P.A.D.; methodology, A.J.Y.; software, A.J.Y.; validation, A.J.Y., C.C.I., J.M.P. and H.C.H.; formal analysis, A.J.Y., and T.K.E.; investigation, D.R., M.M., S.R.N., H.C.H., A.J.Y., and J.M.P.; resources, A.J.Y. and P.A.D.; data curation, A.J.Y., and T.K.E. ; writing—original draft preparation, A.J.Y., and T.K.E.; writing—review and editing, A.J.Y.; visualization, A.J.Y.; supervision, A.J.Y., A.S., C.C.I. and P.A.D.; project administration, A.J.Y.; funding acquisition, A.J.Y. and P.A.D. All authors have read and agreed to the published version of the manuscript.

Funding: This research was supported by the National Science Foundation through the EPSCoR RII Track-1: Emergent Quantum Materials and Technologies (EQUATE), Award OIA-2044049, the Nebraska Materials Research Science and Engineering Center grant No. DMR-1420645, and the Nebraska Nanoscale Facility: National Nanotechnology Coordinated Infrastructure and the Nebraska Center for Materials and Nanoscience, under Award ECCS: 2025298, and the Nebraska Research Initiative. This work was additionally supported by the Nebraska Public Power District through the Nebraska Center for Energy Sciences Research at the University of Nebraska-Lincoln, NCESR grant number 19-SE-2018.

Data Availability Statement: Supplementary materials contain the additional data pertinent to the paper.

Acknowledgments: A.J.Y. would like to acknowledge the support provided by Oklahoma State University in the form of start-up funding which partially supported this work.

Conflicts of Interest: The authors declare no competing financial interest.

References

1. Heo, J. H.; Im, S. H.; Noh, J. H.; Mandal, T. N.; Lim, C. S.; Chang, J. A.; Lee, Y. H.; Kim, H. J.; Sarkar, A.; Nazeeruddin, M. K.; et al. Efficient Inorganic-Organic Hybrid Heterojunction Solar Cells Containing Perovskite Compound and Polymeric Hole Conductors. *Nat. Photonics* **2013**, 7 (6), 486–491. https://doi.org/10.1038/nphoton.2013.80.
2. Kojima, A.; Teshima, K.; Shirai, Y.; Miyasaka, T. Organometal Halide Perovskites as Visible-Light Sensitizers for Photovoltaic. *J. Am Chem. Soc.* **2009**, 131, 6050–6051.
3. Bi, D.; Tress, W.; Dar, M. I.; Gao, P.; Luo, J.; Renevier, C.; Schenk, K.; Abate, A.; Giordano, F.; Correa Baena, J. P.; et al. Efficient Luminescent Solar Cells Based on Tailored Mixed-Cation Perovskites. **Sci. Adv. 2016**, 2 (1), e1501170. https://doi.org/10.1126/sciadv.1501170.
4. Lee, M. M.; Teuscher, J.; Miyasaka, T.; Murakami, T. N.; Snaith, H. J. Efficient Hybrid Solar Cells Based on Meso-Superstructured Organometal Halide Perovskites. *Science (80-.).* **2012**, 338, 643–647. https://doi.org/10.1126/science.1228604.
5. Smith, I. C.; Hoke, E. T.; Solis-Ibarra, D.; McGehee, M. D.; Karunadasa, H. I. A Layered Hybrid Perovskite Solar-Cell Absorber with Enhanced Moisture Stability. *Angew. Chemie - Int. Ed.* **2014**, 53 (42), 11232–11235. https://doi.org/10.1002/anie.201406466.
6. Eperon, G. E.; Paternò, G. M.; Sutton, R. J.; Zampetti, A.; Haghighirad, A. A.; Cacialli, F.; Snaith, H. J. Inorganic Caesium Lead Iodide Perovskite Solar Cells. *J. Mater. Chem. A* **2015**, 3 (39), 19688–19695. https://doi.org/10.1039/C5TA06398A.
7. Liang, J.; Wang, C.; Wang, Y.; Xu, Z.; Lu, Z.; Ma, Y.; Zhu, H.; Hu, Y.; Xiao, C.; Yi, X.; et al. All-Inorganic Perovskite Solar Cells. *J. Am. Chem. Soc.* **2016**, 138 (49), 15829–15832. https://doi.org/10.1021/jacs.6b10227.
8. Chen, Y.; Yi, H. T.; Wu, X.; Haroldson, R.; Gartstein, Y. N.; Rodionov, Y. I.; Tikhonov, K. S.; Zakhidov, A.; Zhu, X.-Y.; Podzorov, V. Extended Carrier Lifetimes and Diffusion in Hybrid Perovskites Revealed by Hall Effect and Photoconductivity Measurements. *Nat. Commun*. **2016**, 7, 12253. https://doi.org/10.1038/ncomms12253.
9. Ilie, C. C.; Guzman, F.; Swanson, B. L.; Evans, I. R.; Costa, P. S.; Teeter, J. D.; Shekhirev, M.; Benker, N.; Sikich, S.; Enders, A.; et al. Inkjet Printable-Photoactive All Inorganic Perovskite Films with Long Effective Photocarrier Lifetimes. *J. Phys. Condens. Matter* **2018**, 30 (18), 18LT02. https://doi.org/10.1088/1361-648X/aab986.
10. Shi, D.; Adinolfi, V.; Comin, R.; Yuan, M.; Alarousu, E.; Buin, A.; Chen, Y.; Hoogland, S.; Rothenberger, A.; Katsiev, K.; et al. Low Trap-State Density and Long Carrier Diffusion in Organolead Trihalide Perovskite Single Crystals. *Science (80-.).* **2015**, 347, 519–522.
11. Saliba, M.; Matsui, T.; Seo, J.-Y.; Domanski, K.; Correa-Baena, J.-P.; Mohammad K., N.; Zakeeruddin, S. M.; Tress, W.; Abate, A.; Hagfeldt, A.; et al. Cesium-Containing Triple Cation Perovskite Solar Cells: Improved Stability, Reproducibility and High Efficiency. *Energy Environ. Sci*. **2016**, 9 (6), 2357–2363. https://doi.org/10.1039/C5EE03874J.
12. Bian, H.; Bai, D.; Jin, Z.; Wang, K.; Liang, L.; Wang, H.; Zhang, J.; Wang, Q.; Liu, S. (Frank). Graded Bandgap $CsPbI_{2+x}Br_{1-x}$ Perovskite Solar Cells with a Stabilized Efficiency of 14.4%. *Joule* **2018**, 2 (8), 1500–1510. https://doi.org/10.1016/j.joule.2018.04.012.
13. Chen, C. Y.; Lin, H. Y.; Chiang, K. M.; Tsai, W. L.; Huang, Y. C.; Tsao, C. S.; Lin, H. W. All-Vacuum-Deposited Stoichiometrically Balanced Inorganic Cesium Lead Halide Perovskite Solar Cells with Stabilized Efficiency Exceeding 11%. *Adv. Mater*. **2017**, 29 (12), 1–7. https://doi.org/10.1002/adma.201605290.
14. Xiao, Z.; Zhao, L.; Tran, N. L.; Lin, Y. L.; Silver, S. H.; Kerner, R. A.; Yao, N.; Kahn, A.; Scholes, G. D.; Rand, B. P. Mixed-Halide Perovskites with Stabilized Bandgaps. *Nano Lett.* **2017**, 17 (11), 6863–6869. https://doi.org/10.1021/acs.nanolett.7b03179.
15. Protesescu, L.; Yakunin, S.; Bodnarchuk, M. I.; Krieg, F.; Caputo, R.; Hendon, C. H.; Yang, R. X.; Walsh, A.; Kovalenko, M. V. Nanocrystals of Cesium Lead Halide Perovskites (CsPbX3, X = Cl, Br, and I): Novel Optoelectronic Materials Showing Bright Emission with Wide Color Gamut. *Nano Lett.* **2015**, 15 (6), 3692–3696. https://doi.org/10.1021/nl5048779.
16. Shekhirev, M.; Goza, J.; Teeter, J.; Lipatov, A.; Sinitiskii, A. Synthesis of Cesium Lead Halide Quantum Dots. *J. Chem. Educ.* **2017**, 94 (8), 1150–1156. https://doi.org/10.1021/acs.jchemed.7b00144.
17. Su, Y.; Chen, X.; Ji, W.; Zeng, Q.; Ren, Z.; Su, Z.; Liu, L. Highly Controllable and Efficient Synthesis of Mixed-Halide CsPbX3(X = Cl, Br, I) Perovskite QDs toward the Tunability of Entire Visible Light. *ACS Appl. Mater. Interfaces* **2017**, 9 (38), 33020–33028. https://doi.org/10.1021/acsami.7b10612.
18. Wang, Y.; Li, X.; Nalla, V.; Zeng, H.; Sun, H. Solution-Processed Low Threshold Vertical Cavity Surface Emitting Lasers from All-Inorganic Perovskite Nanocrystals. *Adv. Funct. Mater.* **2017**, 27 (13), 1–7. https://doi.org/10.1002/adfm.201605088.
19. Wang, Y.; Li, X.; Song, J.; Xiao, L.; Zeng, H.; Sun, H. All-Inorganic Colloidal Perovskite Quantum Dots: A New Class of Lasing Materials with Favorable Characteristics. *Adv. Mater.* **2015**, 27 (44), 7101–7108. https://doi.org/10.1002/adma.201503573.
20. Raghavan, C. M.; Chen, T. P.; Li, S. S.; Chen, W. L.; Lo, C. Y.; Liao, Y. M.; Haider, G.; Lin, C. C.; Chen, C. C.; Sankar, R.; et al. Low-Threshold Lasing from 2D Homologous Organic-Inorganic Hybrid Ruddlesden-Popper Perovskite Single Crystals. *Nano Lett.* **2018**, 18 (5), 3221–3228. https://doi.org/10.1021/acs.nanolett.8b00990.
21. Liu, P.; He, X.; Ren, J.; Liao, Q.; Yao, J.; Fu, H. Organic-Inorganic Hybrid Perovskite Nanowire Laser Arrays. *ACS Nano* **2017**, 11 (6), 5766–5773. https://doi.org/10.1021/acsnano.7b01351.
22. Fu, Y.; Zhu, H.; Stoumpos, C. C.; Ding, Q.; Wang, J.; Kanatzidis, M. G.; Zhu, X.; Jin, S. Broad Wavelength Tunable Robust Lasing from Single-Crystal Nanowires of Cesium Lead Halide Perovskites ($CsPbX_3$, X = Cl, Br, I). *ACS Nano* **2016**, 10 (8), 7963–7972. https://doi.org/10.1021/acsnano.6b03916.

23. Shoaib, M.; Wang, X.; Zhang, X.; Wang, X.; Zhou, H.; Xu, T.; Hu, X.; Liu, H.; Fan, X.; Zheng, W.; et al. Directional Growth of Ultralong CsPbBr3Perovskite Nanowires for High-Performance Photodetectors. *J. Am. Chem. Soc.* **2017**, 139 (44), 15592–15595. https://doi.org/10.1021/jacs.7b08818.
24. Zheng, W.; Xiong, X.; Lin, R.; Zhang, Z.; Xu, C.; Huang, F. Balanced Photodetection in One-Step Liquid-Phase Synthesis CsPbBr 3 Micro/Nanoflake Single Crystal. *ACS Appl. Mater. Interfaces* **2018**, 10, 1865–1870. https://doi.org/10.1021/acsami.7b18093.
25. Dou, L.; Yang, Y. M.; You, J.; Hong, Z.; Chang, W. H.; Li, G.; Yang, Y. Solution-Processed Hybrid Perovskite Photodetectors with High Detectivity. *Nat. Commun.* **2014**, 5, 1–6. https://doi.org/10.1038/ncomms6404.
26. Stoumpos, C. C.; Malliakas, C. D.; Peters, J. A.; Liu, Z.; Sebastian, M.; Im, J.; Chasapis, T. C.; Wibowo, A. C.; Chung, D. Y.; Freeman, A. J.; et al. Crystal Growth of the Perovskite Semiconductor $CsPbBr_3$: A New Material for High-Energy Radiation Detection. *Cryst. Growth Des.* **2013**, 13 (7), 2722–2727. https://doi.org/10.1021/cg400645t.
27. Yakunin, S.; Protesescu, L.; Krieg, F.; Bodnarchuk, M. I.; Nedelcu, G.; Humer, M.; De Luca, G.; Fiebig, M.; Heiss, W.; Kovalenko, M. V. Low-Threshold Amplified Spontaneous Emission and Lasing from Colloidal Nanocrystals of Caesium Lead Halide Perovskites. *Nat. Commun.* **2015**, 6, 1–8. https://doi.org/10.1038/ncomms9056.
28. Frolova, L. A.; Anokhin, D. V.; Piryazev, A. A.; Luchkin, S. Y.; Dremova, N. N.; Stevenson, K. J.; Troshin, P. A. Highly Efficient All-Inorganic Planar Heterojunction Perovskite Solar Cells Produced by Thermal Coevaporation of CsI and PbI_2. *J. Phys. Chem. Lett.* **2017**, 8 (1), 67–72. https://doi.org/10.1021/acs.jpclett.6b02594.
29. Johnston, M. B.; Herz, L. M. Hybrid Perovskites for Photovoltaics: Charge-Carrier Recombination, Diffusion, and Radiative Efficiencies. *Acc. Chem. Res.* **2016**, 49 (1), 146–154. https://doi.org/10.1021/acs.accounts.5b00411.
30. Jeon, N. J.; Na, H.; Jung, E. H.; Yang, T. Y.; Lee, Y. G.; Kim, G.; Shin, H. W.; Il Seok, S.; Lee, J.; Seo, J. A Fluorene-Terminated Hole-Transporting Material for Highly Efficient and Stable Perovskite Solar Cells. *Nat. Energy* **2018**, 3 (8), 682–689. https://doi.org/10.1038/s41560-018-0200-6.
31. Li, C.; Guerrero, A.; Zhong, Y.; Huettner, S. Origins and Mechanisms of Hysteresis in Organometal Halide Perovskites. *J. Phys. Condens. Matter* **2017**, 29 (19), 193001. https://doi.org/10.1088/1361-648X/aa626d.
32. Sutton, R. J.; Eperon, G. E.; Miranda, L.; Parrott, E. S.; Kamino, B. A.; Patel, J. B.; Horantner, M. T.; Johnston, M. B.; Haghighirad, A. A.; Moore, D. T.; et al. Bandgap-Tunable Cesium Lead Halide Perovskites with High Thermal Stability for Efficient Solar Cells. *Adv. Energy Mater.* **2016**, 6, 1502458. https://doi.org/10.1002/aenm.201502458.
33. Kulbak, M.; Gupta, S.; Kedem, N.; Levine, I.; Bendikov, T.; Hodes, G.; Cahen, D. Cesium Enhances Long-Term Stability of Lead Bromide Perovskite-Based Solar Cells. *J. Phys. Chem. Lett.* **2016**, 7 (1), 167–172. https://doi.org/10.1021/acs.jpclett.5b02597.
34. Endres, J.; Kulbak, M.; Zhao, L.; Rand, B. P.; Cahen, D.; Hodes, G.; Kahn, A. Electronic Structure of the CsPbBr3/Polytriarylamine (PTAA) System. *J. Appl. Phys.* **2017**, 121 (3), 035304. https://doi.org/10.1063/1.4974471.
35. Mathies, F.; Eggers, H.; Richards, B. S.; Hernandez-Sosa, G.; Lemmer, U.; Paetzold, U. W. Inkjet-Printed Triple Cation Perovskite Solar Cells. *ACS Appl. Energy Mater.* **2018**, 1 (5), 1834–1839. https://doi.org/10.1021/acsaem.8b00222.
36. Song, J.; Xu, L.; Li, J.; Xue, J.; Dong, Y.; Li, X.; Zeng, H. Monolayer and Few-Layer All-Inorganic Perovskites as a New Family of Two-Dimensional Semiconductors for Printable Optoelectronic Devices. *Adv. Mater.* **2016**, 28 (24), 4861–4869. https://doi.org/10.1002/adma.201600225.
37. Richmond, D.; McCormick, M.; Ekanayaka, T. K.; Teeter, J. D.; Swanson, B. L.; Benker, N.; Hao, G.; Sikich, S.; Enders, A.; Sinitskii, A.; et al. Inkjet Printing All Inorganic Halide Perovskite Inks for Photovoltaic Applications. *JoVE* **2018**, e58760. https://doi.org/doi:10.3791/58760.
38. Bae, S. H.; Zhao, H.; Hsieh, Y. T.; Zuo, L.; De Marco, N.; Rim, Y. S.; Li, G.; Yang, Y. Printable Solar Cells from Advanced Solution-Processible Materials. *Chem* **2016**, 1 (2), 197–219. https://doi.org/10.1016/j.chempr.2016.07.010.
39. Habas, S. E.; Platt, H. a S.; van Hest, M. F. A. M.; Ginley, D. S. Low-Cost Inorganic Solar Cells: From Ink To Printed Device. *Chem. Rev.* **2010**, 110 (11), 6571–6594. https://doi.org/10.1021/cr100191d.
40. Leenen, M. A. M.; Arning, V.; Thiem, H.; Steiger, J.; Anselmann, R. Printable Electronics: Flexibility for the Future. *Phys. Status Solidi Appl. Mater. Sci.* **2009**, 206 (4), 588–597. https://doi.org/10.1002/pssa.200824428.
41. Akkerman, Q. A.; D'Innocenzo, V.; Accornero, S.; Scarpellini, A.; Petrozza, A.; Prato, M.; Manna, L. Tuning the Optical Properties of Cesium Lead Halide Perovskite Nanocrystals by Anion Exchange Reactions. *J. Am. Chem. Soc.* **2015**, 137 (32), 10276–10281. https://doi.org/10.1021/jacs.5b05602.
42. De Roo, J.; Ibáñez, M.; Geiregat, P.; Nedelcu, G.; Walravens, W.; Maes, J.; Martins, J. C.; Van Driessche, I.; Kovalenko, M. V.; Hens, Z. Highly Dynamic Ligand Binding and Light Absorption Coefficient of Cesium Lead Bromide Perovskite Nanocrystals. *ACS Nano* **2016**, 10 (2), 2071–2081. https://doi.org/10.1021/acsnano.5b06295.
43. Mizusaki, J.; Arai, K.; Fueki, K. Ionic Conduction of the Perovskite-Type Halides. *Solid State Ionics* **1983**, 11 (3), 203–211. https://doi.org/https://doi.org/10.1016/0167-2738(83)90025-5.
44. Bi, C.; Wang, S.; Wen, W.; Yuan, J.; Cao, G.; Tian, J. Room-Temperature Construction of Mixed-Halide Perovskite Quantum Dots with High Photoluminescence Quantum Yield. *J. Phys. Chem. C* **2018**, 122, 5151–5160. https://doi.org/10.1021/acs.jpcc.7b12607.
45. Eaton, S. W.; Lai, M.; Gibson, N. A.; Wong, A. B.; Dou, L.; Ma, J.; Wang, L.-W.; Leone, S. R.; Yang, P. Lasing in Robust Cesium Lead Halide Perovskite Nanowires. *Proc. Natl. Acad. Sci.* **2016**, 113 (8), 1993. https://doi.org/10.1073/pnas.1600789113.
46. Koolyk, M.; Amgar, D.; Aharon, S.; Etgar, L. Kinetics of Cesium Lead Halide Perovskite Nanoparticle Growth; Focusing and de-Focusing of Size Distribution. *Nanoscale* **2016**, 8 (12), 6403–6409. https://doi.org/10.1039/c5nr09127f.

47. Palazon, F.; Di Stasio, F.; Lauciello, S.; Krahne, R.; Prato, M.; Manna, L. Evolution of CsPbBr 3 Nanocrystals upon Post-Synthesis Annealing under an Inert Atmosphere. *J. Mater. Chem. C* **2016**, 4 (39), 9179–9182. https://doi.org/10.1039/C6TC03342C.
48. Scherrer, P. Bestimmung Der Größe Und Der Inneren Struktur von Kolloidteilchen Mittels Röntgenstrahlen. In Nachrichten von der Gesellschaft der Wissenschaften zu Göttingen, Mathematisch-Physikalische Klasse; 1918; Vol. 2, pp 98–100. https://doi.org/10.1007/978-3-662-33915-2.
49. Spanjaard, D.; Guillot, C.; Desjonquères, M.-C.; Tréglia, G.; Lecante, J. Surface Core Level Spectroscopy of Transition Metals: A New Tool for the Determination of Their Surface Structure. *Surf. Sci. Rep.* **1985**, 5 (1), 1–85. https://doi.org/https://doi.org/10.1016/0167-5729(85)90003-2.
50. Citrin, P. H.; Wertheim, G. K.; Baer, Y. Core-Level Binding Energy and Density of States from the Surface Atoms of Gold. *Phys. Rev. Lett.* **1978**, 41 (20), 1425–1428. https://doi.org/10.1103/PhysRevLett.41.1425.
51. Wooten, D.; Ketsman, I.; Xiao, J.; Losovyj, Y. B.; Petrosky, J.; McClory, J.; Burak, Y. V.; Adamiv, V. T.; Dowben, P. A. The Surface Core Level Shift for Lithium at the Surface of Lithium Borate. *Phys. B Condens. Matter* **2010**, 405 (1), 461–464. https://doi.org/10.1016/j.physb.2009.08.312.
52. Conings, B.; Baeten, L.; De Dobbelaere, C.; D'Haen, J.; Manca, J.; Boyen, H.-G. Perovskite-Based Hybrid Solar Cells Exceeding 10% Efficiency with High Reproducibility Using a Thin Film Sandwich Approach. *Adv. Mater.* **2014**, 26 (13), 2041–2046. https://doi.org/10.1002/adma.201304803.
53. Lindblad, R.; Jena, N. K.; Philippe, B.; Oscarsson, J.; Bi, D.; Lindblad, A.; Mandal, S.; Pal, B.; Sarma, D. D.; Karis, O.; et al. Electronic Structure of CH3NH3PbX3 Perovskites: Dependence on the Halide Moiety. *J. Phys. Chem. C* **2015**, 119 (4), 1818–1825. https://doi.org/10.1021/jp509460h.
54. Zu, F.; Amsalem, P.; Salzmann, I.; Wang, R.; Ralaiarisoa, M.; Kowarik, S.; Duhm, S.; Koch, N. Impact of White Light Illumination on the Electronic and Chemical Structures of Mixed Halide and Single Crystal Perovskites. *Adv. Opt. Mater.* **2017**, 5 (9), 1700139. https://doi.org/10.1002/adom.201700139.
55. Sadoughi, G.; Starr, D. E.; Handick, E.; Stranks, S. D.; Gorgoi, M.; Wilks, R. G.; Bär, M.; Snaith, H. J. Observation and Mediation of the Presence of Metallic Lead in Organic–Inorganic Perovskite Films. *ACS Appl. Mater. Interfaces* **2015**, 7 (24), 13440–13444. https://doi.org/10.1021/acsami.5b02237.
56. Liu, P.; Liu, X.; Lyu, L.; Xie, H.; Zhang, H.; Niu, D.; Huang, H.; Bi, C.; Xiao, Z.; Huang, J.; et al. Interfacial Electronic Structure at the CH3NH3PbI3/MoOx Interface. *Appl. Phys. Lett.* **2015**, 106 (19), 193903. https://doi.org/10.1063/1.4921339.
57. Komesu, T.; Huang, X.; Paudel, T. R.; Losovyj, Y. B.; Zhang, X.; Schwier, E. F.; Kojima, Y.; Zheng, M.; Iwasawa, H.; Shimada, K.; et al. Surface Electronic Structure of Hybrid Organo Lead Bromide Perovskite Single Crystals. *J. Phys. Chem. C* **2016**, 120 (38), 21710–21715. https://doi.org/10.1021/acs.jpcc.6b08329.
58. Begum, R.; Parida, M. R.; Abdelhady, A. L.; Murali, B.; Alyami, N. M.; Ahmed, G. H.; Hedhili, M. N.; Bakr, O. M.; Mohammed, O. F. Engineering Interfacial Charge Transfer in $CsPbBr_3$ Perovskite Nanocrystals by Heterovalent Doping. *J. Am. Chem. Soc.* **2017**, 139 (2), 731–737. https://doi.org/10.1021/jacs.6b09575.
59. Li, Y.; Shi, Z.-F.; Li, S.; Lei, L.-Z.; Ji, H.-F.; Wu, D.; Xu, T.-T.; Tian, Y.-T.; Li, X.-J. High-Performance Perovskite Photodetectors Based on Solution-Processed All-Inorganic $CsPbBr_3$ Thin Films. *J. Mater. Chem. C* **2017**, 5, 8355–8360. https://doi.org/10.1039/C7TC02137B.
60. Li, M.; Zhang, X.; Lu, S.; Yang, P. Phase Transformation, Morphology Control, and Luminescence Evolution of Cesium Lead Halide Nanocrystals in the Anion Exchange Process. *RSC Adv.* **2016**, 6 (105), 103382–103389. https://doi.org/10.1039/c6ra22070c.
61. Hautala, L.; Jänkälä, K.; Löytynoja, T.; Mikkelä, M. H.; Prisle, N.; Tchaplyguine, M.; Huttula, M. Experimental Observation of Structural Phase Transition in CsBr Clusters. *Phys. Rev. B* **2017**, 95 (4), 1–8. https://doi.org/10.1103/PhysRevB.95.045402.
62. Hautala, L.; Jänkälä, K.; Mikkelä, M. H.; Tchaplyguine, M.; Huttula, M. Surface Site Coordination Dependent Responses Resolved in Free Clusters: Applications for Neutral Sub-Nanometer Cluster Studies. *Phys. Chem. Chem. Phys.* **2015**, 17 (10), 7012–7022. https://doi.org/10.1039/c4cp05422a.
63. Zhang, J.; He, J.; Yang, L.; Gan, Z. Photoluminescent Spectral Broadening of Lead Halide Perovskite Nanocrystals Investigated by Emission Wavelength Dependent Lifetime. Molecules 2020, 25 (5), 1151. https://doi.org/10.3390/molecules25051151.
64. Kang, J.; Wang, L. W. High Defect Tolerance in Lead Halide Perovskite $CsPbBr_3$. *J. Phys. Chem. Lett.* **2017**, 8 (2), 489–493. https://doi.org/10.1021/acs.jpclett.6b02800.
65. Shockley, W.; Read, W. T. Statistics of the Recombinations of Holes and Electrons. *Phys. Rev.* **1952**, 87 (5), 835–842. https://doi.org/10.1103/PhysRev.87.835.
66. Hall, R. N. Electron-Hole Recombination in Germanium. *Phys. Rev.* **1952**, 87, 387.
67. Fitzgerald, D. J.; Grove, A. S. Surface Recombination in Semiconductors. *Surf. Sci.* **1968**, 15 (6), 347–369. https://doi.org/10.1109/T-ED.1968.16296.
68. Lin, H.; Wei, Q.; Wei Ng, K.; Dong, J.-Y.; Li, J.-L.; Liu, W.-W.; Yan, S.-S.; Chen, S.; Xing, G.-C.; Tang, X.-S.; et al. Stable and Efficient Blue-Emitting CsPbBr3 Nanoplatelets with Potassium Bromide Surface Passivation. *Small* **2021**, 17, 2101359.
69. Chang, C. C.; Chi, C. Y.; Yao, M.; Huang, N.; Chen, C. C.; Theiss, J.; Bushmaker, A. W.; Lalumondiere, S.; Yeh, T. W.; Povinelli, M. L.; et al. Electrical and Optical Characterization of Surface Passivation in GaAs Nanowires. *Nano Lett.* **2012**, 12 (9), 4484–4489. https://doi.org/10.1021/nl301391h.
70. Reese, M. O.; Perkins, C. L.; Burst, J. M.; Farrell, S.; Barnes, T. M.; Johnston, S. W.; Kuciauskas, D.; Gessert, T. A.; Metzger, W. K. Intrinsic Surface Passivation of CdTe. *J. Appl. Phys.* **2015**, 118 (15), 382–385. https://doi.org/10.1063/1.4933186.

71. Dey, A.; Rathod, P.; Kabra, D. Role of Localized States in Photoluminescence Dynamics of High Optical Gain $CsPbBr_3$ Nanocrystals. *Adv. Opt. Mater.* **2018**, 6, 1800109. https://doi.org/10.1002/adom.201800109.
72. Hu, F.; Zhang, H.; Sun, C.; Yin, C.; Lv, B.; Zhang, C.; Yu, W. W.; Wang, X.; Zhang, Y.; Xiao, M. Superior Optical Properties of Perovskite Nanocrystals as Single Photon Emitters. *ACS Nano* **2015**, 9 (12), 12410–12416. https://doi.org/10.1021/acsnano.5b05769.
73. Saidaminov, M. I.; Haque, M. A.; Almutlaq, J.; Sarmah, S.; Miao, X. H.; Begum, R.; Zhumekenov, A. A.; Dursun, I.; Cho, N.; Murali, B.; et al. Inorganic Lead Halide Perovskite Single Crystals Phase-Selective Low Temperature Growth, Carrier Transport Properties, and Self-Powered Photodetection. *Adv. Opt. Mater.* **2017**, 5, 1600704.
74. Li, X.; Wu, Y.; Zhang, S.; Cai, B.; Gu, Y.; Song, J.; Zeng, H. CsPbX3 Quantum Dots for Lighting and Displays: Room-Temperature Synthesis, Photoluminescence Superiorities, Underlying Origins and White Light-Emitting Diodes. *Adv. Funct. Mater.* **2016**, 26, 2435–2445.
75. Zhang, D.; Yang, Y.; Bekenstein, Y.; Yu, Y.; Gibson, N. A.; Wong, A. B.; Eaton, S. W.; Kornienko, N.; Kong, Q.; Lai, M.; et al. Synthesis of Composition Tunable and Highly Luminescent Cesium Lead Halide Nanowires through Anion-Exchange Reactions. *J. Am. Chem. Soc.* **2016**, 138 (23), 7236–7239. https://doi.org/10.1021/jacs.6b03134.
76. Han, Q.; Wu, W.; Liu, W.; Yang, Y. The Peak Shift and Evolution of Upconversion Luminescence from CsPbBr3 Nanocrystals under Femtosecond Laser Excitation. *RSC Adv.* **2017**, 7 (57), 35757–35764. https://doi.org/10.1039/c7ra06211g.
77. Chen, J.; Chábera, P.; Pascher, T.; Messing, M. E.; Schaller, R.; Canton, S.; Zheng, K.; Pullerits, T. Enhanced Size Selection in Two-Photon Excitation for $CsPbBr_3$ Perovskite Nanocrystals. *J. Phys. Chem. Lett.* **2017**, 8 (20), 5119–5124. https://doi.org/10.1021/acs.jpclett.7b02178.
78. Wolf, C.; Lee, T. W. Exciton and Lattice Dynamics in Low-Temperature Processable CsPbBr3 Thin-Films. Mater. *Today Energy* **2018**, 7, 199–207. https://doi.org/10.1016/j.mtener.2017.09.010.
79. Lorenzon, M.; Sortino, L.; Akkerman, Q.; Accornero, S.; Pedrini, J.; Prato, M.; Pinchetti, V.; Meinardi, F.; Manna, L.; Brovelli, S. Role of Nonradiative Defects and Environmental Oxygen on Exciton Recombination Processes in $CsPbBr_3$ Perovskite Nanocrystals. *Nano Lett.* **2017**, 17 (6), 3844–3853. https://doi.org/10.1021/acs.nanolett.7b01253.
80. Di Stasio, F.; Christodoulou, S.; Huo, N.; Konstantatos, G. Near-Unity Photoluminescence Quantum Yield in CsPbBr3 Nanocrystal Solid-State Films via Postsynthesis Treatment with Lead Bromide. *Chem. Mater.* **2017**, 29 (18), 7663–7667. https://doi.org/10.1021/acs.chemmater.7b02834.
81. Liu, M.; Zhong, G.; Yin, Y.; Miao, J.; Li, K.; Wang, C.; Xu, X.; Shen, C.; Meng, H. Aluminum-Doped Cesium Lead Bromide Perovskite Nanocrystals with Stable Blue Photoluminescence Used For Display Backlight. *Adv. Sci.* **2017**, 4, 1700335.
82. Zhou, L.; Yu, K.; Yang, F.; Cong, H.; Wang, N.; Zheng, J.; Zuo, Y.; Li, C.; Cheng, B.; Wang, Q. Insight into the Effect of Ligand-Exchange on Colloidal CsPbBr3 Perovskite Quantum Dot/Mesoporous-TiO2 Composite-Based Photodetectors: Much Faster Electron Injection. *J. Mater. Chem. C* **2017**, 5 (25), 6224–6233. https://doi.org/10.1039/c7tc01611e.